PAPER

Amorphous quininium aspirinate from neat mechanochemistry: diffracting nanocrystalline domains and quick recrystallization upon exposure to solvent vapours†‡

Silvina Pagola, [iD] *[a] James Howard,[b] Johannes Merkelbach[c] and Danny Stam[c]

Quininium aspirinate is mechanochemically prepared as a crystalline solid by liquid-assisted grinding, or as an amorphous phase (as determined by X-ray powder diffraction), by neat grinding or neat ball milling. Our previous work demonstrated using FT-IR spectroscopy that a mechanochemical reaction had occurred in the mechanically treated neat mixtures. Herein is reported that microcrystal electron diffraction (microED) afforded the discovery of two diffracting micron-size particles in the amorphous powder synthesized by manual grinding, among a majority of non-diffracting particles. Remarkably, microED data of one of them led to the known lattice parameters of quininium aspirinate. Furthermore, this so-called 'X-ray amorphous' phase quickly recrystallizes upon exposure to vapors of *N,N*-dimethylformamide, or hexane vapours (at a lower rate); but it remains amorphous for longer than 20 months when stored at ambient conditions in a closed container. The lattice parameters and the degrees of crystallinity of both recrystallized materials are identical within the experimental error. However, slightly more intense and better-resolved X-ray powder diffraction peaks are observed in the material recrystallized from *N,N*-dimethylformamide vapours than in the analogous phase recovered from hexane. As expected, Williamson–Hall graphs lead to a larger average crystalline domain size for the former solid. These results illustrate the use of microED for the investigation of structural features in amorphous phases, and the generic role of the solvent vapours in promoting their recrystallization.

Introduction

Often it is important to consistently produce crystalline substances (and even amorphous solids) with specific properties at industrial scales. Properties for which control is sought may be the chemical purity, crystal habit, particle size distribution in powders, polymorphism, chirality, *etc.*, since these could determine the material's performance in subsequent processes, such as chemical reactions, dissolution, powder flow, compaction, *etc.*[1,2] Thus, understanding nucleation, crystal growth, and their kinetics is key. However, although there are theoretical approaches and abundant literature on these topics, knowledge is still lacking.[3–5] In addition to crystalline solids, amorphous solids can be formed since the thermodynamically more stable crystalline state remains kinetically inaccessible. Crystallization from amorphous solids is enabled by overcoming the kinetic barriers.[2,6]

Crystallization and amorphization phenomena are also of interest in the burgeoning field of mechanochemistry. Mechanochemical reactions afford a myriad of advantages in comparison with well-established thermochemistry in solution, such as considerably faster and selective[7] chemical processes (sometimes even reactions not achievable using other synthetic methods), most often directly occurring from solids using minimum amounts of solvents, thus leading to sustainable, "green" chemistry.[8,9] While the number of synthetic procedures using known or new mechanochemical reactions is increasing at unprecedented rates, many physicochemical aspects of mechanochemistry are yet to be fully understood, including their chemical mechanisms.[10] For example, *in situ* monitoring of mechanochemical reactions,[11] recently enabling measurements in ball mills at variable temperatures, involve state-of-the-art methodologies that have led to conspicuous observations in the crystal engineering field (and others). Experimental data has shown a considerable reduction in the polymorphic

[a]Department of Chemistry and Biochemistry, Old Dominion University, 4501 Elkhorn Avenue, Norfolk, VA, 23529, USA. E-mail: spagola@odu.edu

[b]Hampton Roads Academy, 739 Academy Lane, Newport News, VA, 23602, USA

[c]ELDICO Scientific AG, Hegenheimermattweg 167 A, 4123 Allschwil, Switzerland

† The crystallographic information file of quininium aspirinate has been deposited in the Cambridge Structural Database (deposition number 2003354) with refcode IYARUY. The unit cell parameters at 100 K are $a = 8.6256(12)$ Å, $b = 9.6680(13)$ Å, $c = 30.557(4)$ Å, $\alpha = \beta = \gamma = 90°$, in the space group $P2_12_12_1$ (no. 19), orthorhombic.

‡ Electronic supplementary information (ESI) available. See DOI: https://doi.org/10.1039/d5mr00028a

transition temperatures of organic solids, by up to 31 °C,[12,13] in comparison with the thermodynamic transition temperatures in absence of ball milling. However, explanations at the fundamental physical chemistry level, using a theoretical framework fully describing the combined effects of thermal and mechanical activation enabling such observations (and many others inherent to mechanochemical reactivity and mechanisms),[14,15] plus the prediction of similar phenomena, are rather at the stage of emerging experimental verifications[16] and are yet far from mature.

Likewise, little is known about the nucleation and crystal growth processes occurring during mechanochemical reactions,[10] such as by ball milling powders. Nonetheless, sometimes relevant information could be inferred if the kinetic model for the reaction[17] has been determined. Since nearly a decade ago, pioneer measurements applying recently developed methodologies have led to *in situ* monitoring of mechanochemical reactions in ball mills by synchrotron X-ray powder diffraction (XRPD),[18,19] Raman spectroscopy,[20,21] and thermography,[22] sometimes combined. Often the reactants are mechanically treated together with small volumes of liquid additives, a method called liquid-assisted grinding (LAG).[23,24] The particle morphologies and their size distribution in the powdered products, the preferred orientation/texture, crystalline domain size, microstrain, and degrees of crystallinity, all considerably vary among mechanochemical reactions, and the experimental conditions used. The latter include (among others) the temperature, the amount of energy applied through a mechanical treatment per time unit, and the treatment's duration.

It is empirically well established that LAG enhances the crystallinity of the products.[23,24] However, fundamental level explanations of LAG effects are lacking, and these vary from reaction to reaction.[23] In our previous work involving charge transfer complexes of tetrathiafulvalene,[25–27] LAG led to higher degrees of crystallinity (reduced amorphous content) and larger crystalline domain sizes, giving rise to sharper X-ray powder diffraction (XRPD) peaks and lower amorphous halos than those for the products of neat mechanochemical syntheses. This in turn, substantially facilitated crystal structure determination from XRPD, especially using synchrotron XRPD data.

Whilst most crystal structures are determined using single crystal X-ray diffraction, there is growing interest in microcrystal electron diffraction (microED)[28–31] due to recent developments in improved methodologies and dedicated hardware,[32,33] making it a remarkably effective technique to circumvent the need of growing single crystals of suitable size and quality for structural analysis. MicroED has been successfully used for the structural characterization of macromolecular compounds,[31] small-molecule organics,[34] metal–organic, and inorganic materials,[35] from nano- to micron-sized crystallites. These include also mechanochemical products such as 2-aminopyrimidine:succinic acid cocrystals,[36] transition metal complexes,[35,37] and pharmaceuticals.[38–40] As a plus, the determination of hydrogen positions from Fourier difference maps is also possible.[41] Phenomena such as tautomerism and hydrogen disorder, H atoms attached to heavy atoms in hydrides,[35] or the

unambiguous identification of salts or cocrystals, all benefit from experimental hydrogen positions, which are generally not obtainable from XRPD (laboratory or synchrotron), or from neutron powder diffraction (unless organic solids are deuterated, or their H content is low), due to the incoherent fraction of hydrogen's scattering length. Additionally, dynamical refinements of microED data can provide insights into absolute stereochemistry from studies in microcrystalline or even nanocrystalline materials.[42,43]

Crystalline solids can be rendered amorphous upon milling.[44,45] The application of mechanical treatments leads to the accumulation of lattice defects, that cause the disruption and eventual loss of the long-range order.[46] XRPD reveals these processes through the broadening of the diffraction peaks, and the increase of the intensity of the amorphous halos.[47] Pharmaceuticals (and other industrially significant solids) are often processed by milling to modify properties of interest (*e.g.*, reduce particle sizes to increase dissolution rates), and so they can become amorphous.[44] Amorphous phases are typically more soluble than their crystalline counterparts; however, their disadvantage in pharmaceutical applications is that they may recrystallize upon processing or storage. Amorphous phases are non-equilibrium systems, and their properties depend on how the amorphous state was obtained. Nonetheless, various amorphization processes can be applied to pharmaceuticals, such as melt quenching, hot melt extrusion, freeze and spray drying, lyophilization, and cryo-milling.[48] However, the resulting amorphous phases must be stabilized against crystallization.[2,48]

Moreover, crystallization from amorphous solids is often different than that from solutions[49] or quenched liquids. Amorphous phases obtained by milling may recrystallize into different polymorphs by heating, or with different kinetics than the corresponding quenched liquids, pointing to differences in nucleation processes.[44] For example, a non-classical crystallization mechanism from amorphous cyclosporin A, involving the formation of mesostructured aggregates, crystallographic reorientation, and particle attachment, has been experimentally demonstrated by time-resolved cryogenic transmission electron microscopy (cryo-TEM) and XRPD.[49]

Our current work reports the study of amorphous quininium aspirinate (QA), a drug–drug salt of the antimalarial drug quinine and the non-steroidal anti-inflammatory drug (NSAID) aspirin,[50] using microED, XRPD, and optical microscopy. This study contributes to our understanding of the amorphous states obtainable by mechanochemistry, and their recrystallization processes upon exposure to organic solvents. These results additionally point to new opportunities for the characterization of organic and other amorphous phases by microED.

Experimental

Materials and synthesis

A finely divided powder of (–)-quinine +98.0% purity, and crystalline aspirin +99.0% purity were purchased from Sigma. *N,N*-Dimethylformamide (DMF) 99% purity, and hexane (mixture of isomers) 99% purity, were both purchased from Fisher

Scientific. All reactants except aspirin were used as received. Neat aspirin was ball milled before the reactions to reduce crystallite sizes for 30 min at 30 Hz milling frequency, with one steel ball of 6 mm diameter, in a 14 mL acrylic jar. The sample studied by microED at ELDICO Scientific AG was prepared by manually grinding in an agate mortar with pestle 6.0×10^{-5} moles (0.0108 g) of aspirin and 6.0×10^{-5} moles (0.0195 g) of quinine, for 30 minutes under air, at room temperature (RT).

For the recrystallization experiments upon exposure to air only, and the first set of exposures to DMF (measured in days), QA powders were prepared as amorphous phases by XRPD, by manually grinding 2.18×10^{-4} moles (0.0707 g) of quinine and 2.18×10^{-4} moles of aspirin (0.0393 g) in an agate mortar with pestle, at RT under air, for 30 minutes. Grinding was repeated once, also for 30 min. For QA recrystallization experiments upon exposure to DMF (second set of experiments, measured in hours) and hexane vapours, 1.09×10^{-4} moles (0.0354 g) of quinine were manually ground with 1.09×10^{-4} moles (0.0197 g) of aspirin for 30 minutes, at RT under air.

X-ray powder diffraction (XRPD)

XRPD data was collected in a Bruker AXS D2 Phaser X-ray powder diffractometer with Cu Kα radiation and θ–θ configuration, equipped with a LynxEye position sensitive detector (PSD), at RT and under air. The sample holders were rotated at 15 rpm around an axis perpendicular to the powder surface, and a 1 mm air-scattering screen was placed above the sample stage. Soller slits of 2.5° opening were used in the incident and diffracted beams. The datasets for crystal phase identification started at $2\theta = 3°$ and ended at 50°. A 0.6 mm divergence slit was used on the incident beam, while a 3 mm anti-scattering slit, a Ni filter, and a 0.5° PSD opening were used in the diffracted beam. XRPD data was collected in continuous scan mode, in 0.02° 2θ steps, using 1 s counting time per step.

XRPD datasets were graphically represented using DIFFRAC.EVA software[51] unless otherwise indicated. The degree of crystallinity values were automatically calculated by DIFFRAC.EVA in the 3–50° 2θ interval, using automatically estimated backgrounds.

The XRPD datasets for the calculation of unit cell parameters of the recrystallized QA and Williamson–Hall graphs, were collected from $2\theta = 5°$ up to 60° (using a 1 mm air-scattering screen), and from 55° up to 130° using a 3 mm air-scattering screen, with a counting time of 15 s per step for both angular regions. Both datasets were merged using DIFFRAC.EVA software.[51] LaB$_6$ powder (Sigma-Aldrich, 10 μm particle size, 95% purity) was used as an internal standard for peak shape and peak position. The degrees of crystallinity were automatically calculated in the 5–130° 2θ interval.

For the Williamson–Hall graphs, the peak broadenings (as integral breadths[52]) of sample-related origin for eight QA peaks with Miller indices hkl, labelled $\beta_{QA,hkl}$, were calculated from the full width at half maximum (FWHM) values reported in the reflection file output generated by the software GSAS,[53] herein labelled FWHM$_{total,hkl}$. LaB$_6$ (peak shape and peak position internal standard) was used to estimate the instrumental

contribution to peak broadening, labelled FWHM$_{ins}$. The LaB$_6$ peak at 21.35° (closest to the QA maximum intensity at 13.84°) was used for all QA peaks. Thus,

$$\beta_{QA,hkl}{}^2 = \text{FWHM}_{total,hkl}{}^2 - \text{FWHM}_{ins}{}^2$$

Relevant values are summarized in Tables S1 and S2 of the ESI.‡ The linear regressions in Fig. 6 were calculated with the software Grapher®.[54]

Microcrystal electron diffraction (microED)

MicroED data was collected using an ELDICO ED-1 electron diffractometer at RT, under high vacuum (4×10^{-7} kPa). The Eldix software,[55] a LaB$_6$ source at an acceleration voltage of 160 kV ($\lambda = 0.02851$ Å), and a DECTRIS QUADRO® hybrid-pixel detector were also used. QA powders were finely dispersed onto a standard TEM grid (amorphous carbon on Cu). Crystallites were located and centred in Scanning Transmission Electron Microscopy (STEM) imaging mode, and the electron diffraction data was recorded in continuous rotation mode. Data was collected from powder particles of around 1 to 2 μm sizes, using an 800 nm diameter beam. The data was analysed using the APEX4 software.[56]

Optical microscopy

Optical micrographs were obtained using an AmScope MD35 optical microscope equipped with a 640 × 480 pixels USB digital camera. The measurement system was calibrated with a standard ruler slide graduated to 0.1 μm.

Exposure to solvent vapours

Amorphous QA powders were exposed to vapours of either hexane (mixture of isomers) or DMF, at RT in all cases. After confirming with XRPD the presence of amorphous phases, 0.0348 g of QA were mixed with 10.0 mg of LaB$_6$ (used as an internal standard for peak shape and peak position). The mixtures were loaded onto 1.5 cm diameter x 0.5 mm depth cavities on silicon wafers, inserted on Bruker AXS acrylic sample holders for XRPD. These are shown in Fig. S1 (ESI).‡ The powders were placed inside glass jars with metal lids, that also contained a glass vial with approximately 2.5 mL of hexane or DMF. The lids were tightly closed, and the closures were covered with Parafilm® wrap. Liquid solvent was always present in the vials during vapour exposure experiments.

Amorphous QA was exposed to DMF vapours for time intervals first counted in days, and later in hours in a second set of experiments. Exposure to hexane vapours occurred for intervals of 1, 17.5, 67, 92, 134, 233, 282, 325 and 396 hours, computed from the time at which the first exposure started. XRPD data was collected during 40 min immediately after completing the exposures with the times above reported. Once data collection finished, exposure to the same solvent vapour continued immediately.

Results and discussion

MicroED study of the amorphous phase at the single-particle level

Our previous work reported the mechanochemical synthesis and solid-state characterization of QA by XRPD, single crystal X-ray diffraction, thermogravimetry, differential scanning calorimetry, and FT-IR spectroscopy.[50] In brief, LAG with water, ethanol, toluene, or heptane gives rise to crystalline QA (one polymorph so far discovered). FT-IR spectroscopy was used to demonstrate that neat ball milling or manual grinding also produce a mechanochemical reaction, but the products are amorphous phases, as determined by XRPD.

As part of the current work, QA powders prepared by neat manual grinding were analysed with STEM and microED, with the objective of characterizing amorphous QA at the single-particle level, in addition to the traditional laboratory XRPD measurements assessing bulk phase properties. Fig. 1 shows the XRPD data of the sample also investigated by STEM and microED. Although two weak and broad diffraction peaks are detected, they were identified as unreacted aspirin. The most intense diffraction peak of crystalline QA at $2\theta = 13.84°$ (and all QA peaks) are absent, confirming the absence of crystalline QA.

Fig. 2(a) shows two STEM images of this material. Aggregates of round particles of the same morphology, with sizes in the 0.5–3 μm range are observed. A total of thirty-five spots were checked by microED. Twenty-nine showed no diffraction (as expected), but four particles showed some diffracted intensity. Remarkably, two particles gave rise to medium diffracted intensities and resolution. Their electron diffraction data is shown in Fig. 2(b), whilst data from selected fully amorphous particles is shown in Fig. 2(c).

Since diffraction phenomena in powders are observable at the micro- or nano-size crystallite level,[57] these observations have fundamental implications for fully understanding the structural characteristics of amorphous solids in general. Impressively, microED has led to structural data at the atomic
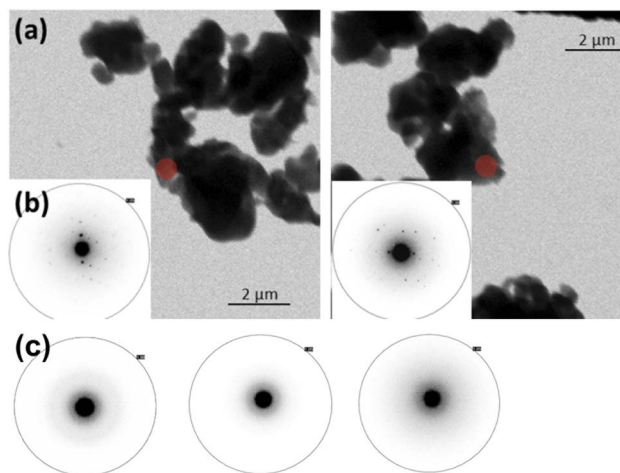

Fig. 2 (a) Scanning Transmission Electron Microscopy (STEM) images of powdered quininium aspirinate showing particle agglomerates. (b) MicroED data of two diffracting particles located at the positions of the red circles in (a). For comparison purposes, the electron diffraction data of amorphous particles is shown in (c).

resolution even from nanocrystals of less than 300 nm thickness.[31,58] Moreover, 3D nano-crystallography techniques based on electron (or X-ray) diffraction offer opportunities to investigate the spatial variability of structural features within crystals, and the unique imperfections and defects existing in nano-crystalline solids, which often elude the methodology used for studying well-ordered crystalline solids.[59]

Observations comparable to those above reported have been made upon the study of an amorphous precipitate of the ethylene insertion product of a dimeric Pt(I) complex upon treatment with ethylene in a THF solution,[35] leading to a very reactive material with an uncommon molecular structure, wherein an ethylene molecule is inserted between Pt ions. Additionally, the structure of the Schwartz's reagent, chloridobis (η^5-cyclopentadienyl) hydridozirconium (a zirconium hydride) was determined from a seemingly amorphous commercial powder.[35]

Hence, although not the first experimental observations of this kind, these could be still regarded as paradigm-shifting observations, unambiguously revealing poorly known, yet possible, long-range order in amorphous solids (including those prepared by mechanochemistry), not detectable with XRPD. The amorphous phases investigated in this study are perhaps better labelled as 'X-ray amorphous' phases.

How do these results conform to currently accepted knowledge? Whilst vibrational and rotational movements are allowed in solids, translational atomic or molecular motions (as in fluids), are insignificant. Our current understanding of the structures of amorphous phases at the atomic/molecular level states that a short-range order in the atomic positions exists, but a long-range order (crystal lattice periodicity) is absent. Two main descriptions of the atomic/molecular connectivity and the 'structures' of amorphous phases are used, the "*random close packed*" and the "*continuous random network*" models.[47,48] In the former, translational, rotational, and conformational symmetry
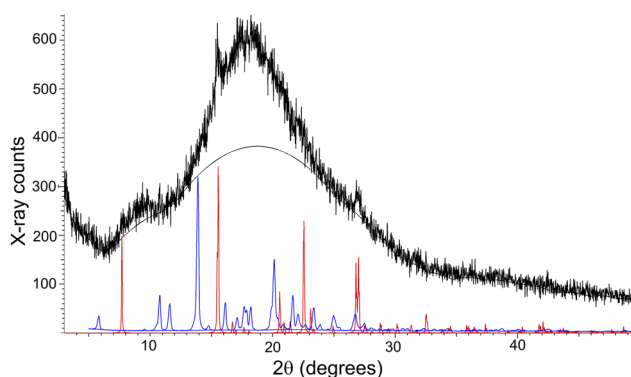

Fig. 1 X-ray powder diffraction data of amorphous QA (black line). An automatically estimated background by DIFFRAC.EVA software[51] is also shown as a black line. For comparison purposes, the diffraction patterns in red and blue correspond to aspirin and quinine, respectively. A small amount of unreacted aspirin was identified by XRPD in this powder, also used in STEM and microED experiments.

could be absent, whilst in the continuous random network model, the atomic positions show a high degree of correlation, so the array can be characterized by its similitude to an 'optimum' packing motif (a crystal structure), which nonetheless, is not fully achieved in the amorphous state. All atoms/molecules may have the same number of neighbours, but instead of well-defined distances and angles (as in a crystalline solid), distributions of those values exist (except for intramolecular covalent bonds). If the molecules are flexible, they would not all have the same conformations in the amorphous state.[48]

Amorphous phases exist for materials with all types of chemical bonding.[6] Although amorphous solids (as bulk phases) do not diffract X-rays due to the lack of long-range order, they can be structurally characterized by pair distribution function (PDF) measurements.[47,60] PDF leads to data comparable to a histogram of interatomic distances, and the probability of finding an atom at a particular distance from another atom. For most organic solids, short-range order is not expected to extend beyond next neighbours, or next nearest neighbour molecules, which would be in the order of 25 Å (or less) for small organic molecules.[47] Nonetheless, it must be noted that the amorphous halos and very broad peaks measured by XRPD, or/and the absence of diffraction peaks in broad angular regions, can be also used for the identification of poorly crystalline organic solids, such as pharmaceutical excipients like microcrystalline cellulose.[60]

An interesting topic is the possible average sizes of the crystalline domains in QA that scatter radiation coherently, thus leading to diffraction phenomena. It has been stated that the XRPD patterns of truly amorphous phases and nanomaterials with diameters smaller than 2 nm can appear similar.[61] Hence, as a rough estimation, the average size of the coherently diffracting domains in this 'X-ray amorphous' material is expected to be in the nanometre range.

MicroED is already established as a valuable addition to the modern structural characterization toolbox. As is often the case following the development of new techniques, opportunities for new studies leading to new understanding emerge. Studies at the single particle level like this one can be very valuable when the properties of the powder are of main interest, and certain structural features such as site vacancies, solvation/desolvation states, compositional and static disorder, structural imperfections, or any other structure-related powder property that is not fully reproducible upon single crystal growth need to be characterized (*e.g.*, for nanomaterials, zeolites, heterogeneous catalysts, naturally occurring minerals, superconducting materials, amorphous pharmaceuticals, mechanochemical products not obtainable as single crystals, *etc.*). Moreover, what advantages could be found in the study of solid solutions, or chiral systems? How the structural characteristics of organic X-ray amorphous phases prepared by various methods may differ? Would it be possible to find nuclei of different polymorphs in them? *etc.*

The discoveries using microED at the single-particle level do not end here. Remarkably, it was also possible to determine a set of unit cell parameters from one of the diffracting crystallites. The values obtained were close to the lattice previously

Table 1 Unit cell parameters for crystalline QA by XRPD[50] and microED (this work), in both cases at RT

Lattice parameter	XRPD	Micro-ED[a]
a (Å)	8.748 (3)	8.92
b (Å)	9.711 (3)	9.71
c (Å)	30.463 (11)	30.33
α (°)	90	90.33
β (°)	90	90.43
γ (°)	90	89.93

[a] Unavailable standard uncertainties. The crystal system was not yet restricted to orthorhombic.

determined for crystalline QA[50] using a Le Bail fit[62] in the space group $P2_12_12_1$, orthorhombic. Note that successfully indexing crystallites by microED is a crucial step in confirming the crystallinity of major reaction products, as crystalline contaminations, impurities, starting materials, or reaction by-products could be mistaken for them. For comparison purposes, the indexing results are summarized in Table 1. The reciprocal lattice and several microED precession images are shown in Fig. 3.

Furthermore, the diffracting particles found by microED could be considered QA nuclei that have not been able to grow sufficiently into a bulk crystalline phase by neat mechanochemistry. This could be tentatively explained as due to the existence of a high viscosity medium in/during ball collisions that trap the reactants and lead to mechanochemical products, from which this amorphous phase could only be formed, in the absence of a liquid additive that would facilitate nuclei growth leading to crystalline QA.

Amorphous recrystallization upon exposure to DMF and hexane vapours

Vapour diffusion into solids and isotopic exchange have been experimentally confirmed. Nakamatsu *et al.* have shown by FT-IR spectroscopy that powders of *rac*-2,2′-dihydroxy-1,1′-binaphthyl exposed to MeOD vapours exchange H by D in the –OH group, showing new bands only after 10 min of exposure, while half of the molecules are deuterated after 120 min.[63] Their work and others have reported so-called "*vapour digestion*" reactions, such as the cocrystallization of pharmaceuticals upon exposure to moisture,[64] and the selective formation of different product stoichiometries by using protic or aprotic solvent vapours.[65] Moreover, the Friščić group has outlined several "*accelerated ageing*" synthetic methods with examples of their applications, not only including vapor digestion syntheses, but also related "green" synthetic approaches from solid reactants, avoiding solvents (or only using solvent vapours), and distinctively requiring minimal energy inputs.[66]

Amorphous phases can recrystallize upon exposure to organic solvents or water. Water sorption on pharmaceutical solids including excipients is routinely studied to understand potential chemical or physical instabilities.[67] While the study of mechanistic aspects of vapour digestion reactions involving organic solvents is not common, it has been hypothesized that
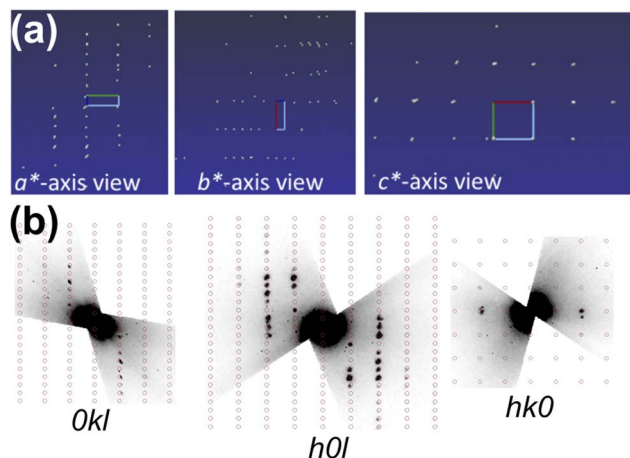
Fig. 3 (a) Views of the reciprocal lattice by microED as shown by the APEX4 software.[56] (b) MicroED precession images showing the diffracted electron beams surrounded by the expected spot positions (red circles) according to the lattice in Table 1, for the orientations indicated in the figure.
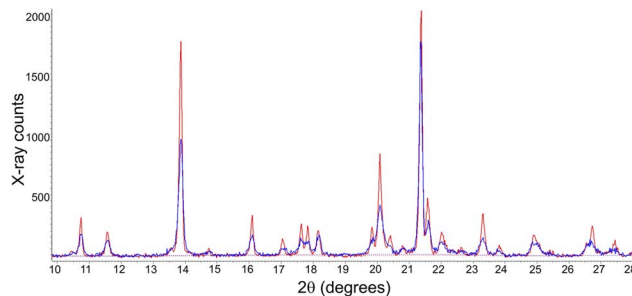

Fig. 4 Overlay of the low angle (10–28°) XRPD data of QA recrystallized from initial amorphous phases upon exposure to DMF vapours for 1 hour (red line), and to hexane vapours for 17.5 hours (blue line). The most intense peak at $2\theta = 21.36°$ corresponds to LaB_6 (internal standard). The material recrystallized from DMF shows more intense, sharper, and better-resolved peaks. This is mainly due to a larger average crystalline domain size.

the solvents enable the formation of mobile phases (at least around crystallite surfaces) wherein chemical reactions can take place, facilitated by the dissolution of one or more reactants.[68]

Vapour exposure experiments on amorphous QA were carried out to study the recrystallization kinetics, at least semi-quantitatively. Interestingly, the amorphous phases exposed only to air at ambient conditions have not recrystallized after more than 20 months of their preparation date (see Fig. S3‡). However, a very weak peak at the 2θ position of the maximum QA intensity was detected in some of the patterns after 11 week of storage. This feature is shown in Fig. S4.‡

This result can be explained on the following basis. One of the most important factors determining the stability of organic amorphous phases is molecular mobility.[48] A rule of thumb for avoiding the recrystallization of pharmaceutical amorphous phases at the year's timescale is their storage at temperatures around 50 K below their glass transition temperature.[67] Thus, these results are not surprising, since the glass transition in QA occurs at around 100 °C,[50] and molecular mobility processes at RT could be considerably restricted.

In contrast, the powders exposed to DMF and hexane vapours quickly recrystallized to the known QA crystal structure. A first set of DMF exposure experiments showed an initial 41% amorphous content determined from the XRPD pattern (note that the crystalline fraction is due to LaB_6) using DIFFRAC.EVA. This was reduced to 13% after 2 days of DMF exposure, and it remained essentially unchanged at 7 days. The XRPD data is shown in Fig. S5.‡ Due to this fast recrystallization timeframe, the exposure times were reduced from days to hours in a second set of experiments, also using DMF. These showed an initial amorphous content of 44%, which remarkably decreased to 15% within only one hour of exposure to DMF vapours. The XRPD data is shown in Fig. S6.‡

Hexane vapours were slower than those of DMF to induce the recrystallization of amorphous QA. Nonetheless,

recrystallization also occurred spontaneously. The initial 44% amorphous QA fraction remained unchanged after the first hour, but it was reduced to 17% after an exposure time of 17.5 hours. The XRPD data is shown in Fig. S7.‡

Although these initial measurements only describe semi-quantitatively an overall faster recrystallization kinetics when DMF is used, the XRPD data of QA recrystallized from DMF systematically shows slightly more intense, sharper, and better-resolved diffraction peaks than the analogous phase recrystallized from hexane. This is shown in Fig. 4. XRPD peak broadening is due to a combination of microstrain due to lattice defects, and small average crystalline domain sizes.[52] The latter must not be confused with 'particle' sizes measurable by microscopy techniques.

Optical microscopy of the recrystallized phases

Selected micrographs of the recrystallization products using DMF and hexane vapours are shown in Fig. 5. Most particles are approximately spherical in shape, with typically less than 3 μm diameter (comparable to STEM results from the amorphous material shown in Fig. 2). They also form agglomerates. Fewer large particles with other shapes were also seen in the sample exposed to DMF (first set of experiments), although the visualization of particle shapes and sizes can never be exhaustive. A
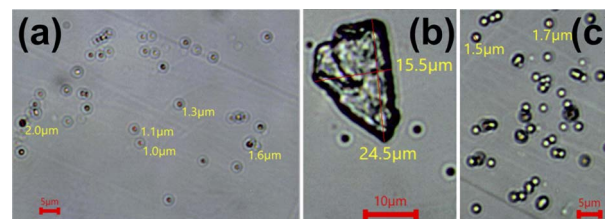

Fig. 5 Optical micrographs of powder particles after recrystallization of amorphous QA upon exposure to vapours of DMF (a) and (b); or hexane (c). In both materials, the particles are typically round with diameters less than 3 μm (see also Table 2). Particle agglomerates are commonly seen. A particle larger than average is shown in (b).

Table 2 The average and the median of the longest dimension of one hundred particles of recrystallized QA, observed under the optical microscope. The vapours inducing recrystallization of each amorphous powder are indicated

Vapour	Average size (μm)	Median size (μm)
DMF	3.00	2.7
Hexane	2.16	2.0

larger-than-average particle is shown in Fig. 5(b). The sizes of these large particles suggest (although this is only a hypothesis), a possible crystallite/particle attachment process by merging interfaces within particle agglomerates, possibly aided by QA dissolution and molecular diffusion on the particle surfaces. The longest dimensions of one hundred particles of each material (excluding agglomerates) were recorded. Their average and median values (which are very similar) are shown in Table 2.

Lattice parameters, degree of crystallinity, and microstructure

XRPD scans with high counting statistics (see Experimental section) were used to determine and compare the unit cell parameters, the final degrees of crystallinity observed, and the microstructure features of both vapour exposure products.

Differently than for the data shown in Fig. 4, the intensity and peak width differences have considerably decreased, nonetheless, some remain. The complete patterns and a zoom of the low-angle regions are shown in Fig. S8.‡

The final degree of crystallinity of the samples exposed to DMF and hexane is the same, 93%. Since most powders contain a small amorphous fraction, this suggests that the recrystallization phase transition is likely completed (or very close to completion).

Le Bail fits[62] of both XRPD datasets were carried out to calculate the unit cell parameters of both recrystallized phases. The fits and low-angle sections of them are shown in Fig. S9 and S10‡ (for QA recrystallized from DMF vapours), and Fig. S11 and S12‡ for the corresponding phase recrystallized from hexane. Table 3 shows the lattice parameters of both materials, which are essentially equivalent within the experimental error. These results additionally imply that DMF and hexane molecules have

not been incorporated into the QA crystal lattices, as this can occur in materials with structural voids accessible to solvent molecules or water.[2]

Thus, besides the overall faster recrystallization kinetics using DMF vapours, the largest difference between these two powdered recrystallization products is found in their microstructures. The latter are typically studied by determining the average crystalline domain size (D) using the Scherrer equation,[52,69] stating that the peak broadening related to sample characteristics (β) is inversely proportional to D, as:

$$D = \frac{K\lambda}{\beta \cos \theta}$$

where θ is half of the peak position in 2θ, K is a constant (0.89 for spherical particles), and λ is the X-ray wavelength (0.15444 nm). Note that β (calculated as described in the Experimental section) is expressed in radians, and the peak of maximum intensity can be used. Alternatively, the Williamson–Hall method[70,71] uses β of several peaks to estimate D, in addition to the lattice microstrain parameter (ε), since microstrain additionally broadens the peaks as a function of the tangent of θ.[71] Thus,

$$\beta = \beta_{size} + \beta_{strain} = \frac{K\lambda}{D \cos \theta} + 4\varepsilon \tan \theta$$

Since $\tan \theta = \sin \theta / \cos \theta$, Williamson–Hall's equation is obtained by multiplying the above equation by $\cos \theta$. A graph representing $\beta \times \cos \theta$ as a function of $4 \times \sin \theta$ leads to values for ε and D from the slope and the intercept, respectively.

Fig. 6 shows the Williamson–Hall graphs for both QA recrystallization products using DMF and hexane. Details of the fits of the diffraction peaks used in the calculations (medium to high intensity, and reasonably non-overlapped in 2θ) are shown in Fig. S10 and S12‡ for DMF and hexane, respectively. Although at least two peaks deviate from a linear relationship (but in opposite fashions), the values determined for D and ε are summarized in Table 4.

Table 3 The unit cell parameters a, b, and c, the lattice volume (V), and the degree of crystallinity (DOC) for QA powders recrystallized from DMF and hexane. R_{wp} and χ^2 agreement factors of both Le Bail fits are also indicated

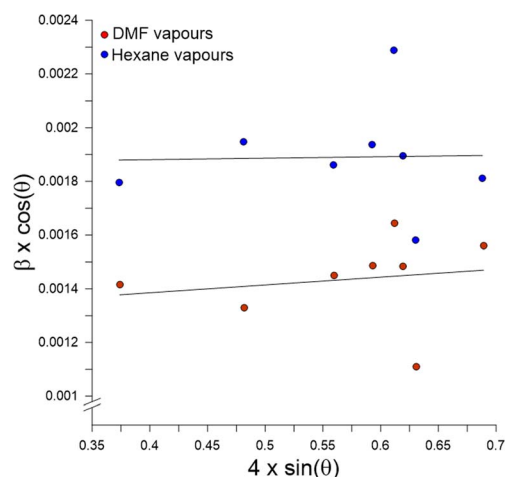| Lattice parameter	DMF	Hexane
a (Å)	8.7353(5)	8.7375(4)
b (Å)	9.7036(3)	9.7032(1)
c (Å)	30.439(2)	30.441(1)
V (Å^3)	2580.2(2)	2580.9(2)
DOC (%)	93	93
R_{wp} (%)	7.22	7.07
χ^2	1.88	1.78

Fig. 6 Williamson–Hall graphs corresponding to QA recrystallized from DMF and hexane vapours. The lines represent the linear fits used to calculate the values reported in Table 4.

Table 4 Williamson–Hall parameters D and ε for QA powders recrystallized from DMF and hexane

Parameter	DMF	Hexane
D (nm)	106	72
ε	30×10^{-5}	5×10^{-5}

The Williamson–Hall method involves approximations, and the above parameter values should be analysed with caution. Nonetheless, the graphs are useful to evaluate trends. Keeping this in mind, the results in Table 4 and Fig. 6 indicate that recrystallization of QA by exposure to DMF leads to a larger average crystalline domain size than hexane, and both are roughly in the hundred-nanometre order of magnitude. The larger differences in XRPD peak intensities and peak widths shown in Fig. 4 (compare with Fig. S8‡), can be explained by a faster nuclei growth into larger crystalline domains in the material exposed to DMF than in the analogous powder exposed to hexane. However, whether additional nuclei could be formed upon vapour exposures has not been experimentally investigated.

Several aspects may be relevant in a discussion toward interpreting all these observations. (1) Solubility differences: the solubility of QA (a hydrogen-bonded salt) in DMF (a polar solvent) should be larger than in hexane (a non-polar liquid), in which QA must be essentially insoluble. This is expected to affect the fraction of QA mobile molecules, thus enhancing the rates of processes requiring molecular diffusion and unrestricted molecular movements, such as the recrystallization of amorphous QA.

Although not observed in this study, different solvents could lead to the crystallization of different polymorphs, and it is possible to screen for organic polymorphs in this manner.[27] A study like this one reports that amorphous indomethacin (prepared by melt quenching) recrystallizes upon exposure to vapours of alcohols of different chain lengths, for 2 hours at 30 °C. Exposure to ethanol favoured the formation of the α-indomethacin form, while 1-octanol led to the γ-polymorph.[72] The recrystallization of both polymorphs followed a kinetic model implying that the rate-determining process is crystal growth at a two-dimensional interface.

(2) Phase transition energetics: the molecules of the solid, the liquid (or solvent), and its vapour, constantly exchange energy. Once the amorphous is reached by volatile molecules that become physically or chemically adsorbed, or dissolve the solid to some extent (for example on particle surfaces), the mobility of QA molecules will increase. The liquid becomes something comparable to a tool to 'kinetically unlock' the phase transition to the thermodynamically stable crystalline solid, which does not happen in amorphous QA only exposed to air in closed containers. Recrystallization upon exposure to DMF or hexane vapours occurs spontaneously at RT (implying $\Delta G < 0$ and $\Delta H < 0$), where G and H are the thermodynamic Gibbs energy and the enthalpy, respectively, and ΔS (S being the entropy) has been neglected. The enthalpy change of vaporization of hexane at 309 K is (30.9 ± 0.1) kJ mol^{-1}, and that for

DMF is 49.2 kJ mol^{-1} at 316 K, whilst the enthalpy changes of adsorption are deemed to be slightly exothermic. One can think of a dynamic phase equilibrium between the vapour (DMF or hexane) and its adsorbed/dissolving liquid, through which the vaporization of the liquid (endothermic, as above) from the powder, occurs at the expense of removing energy of the surrounding QA molecules. Thus, the crystallization process could be thermodynamically driven by the overall exothermic enthalpy change due to 'ordering' the molecules of the amorphous phase into the thermodynamically more stable crystalline solid. In such a scenario, energy-related considerations concerning QA solubility might be only minor, supporting the observation that recrystallization also occurs with hexane vapours (although at a lower rate), even though QA must be essentially insoluble in hexane.

(3) Intermolecular interactions and structure–property relationships: QA's crystal structure is made of zig–zag chains composed of quininium cations linked through hydrogen-bonded quinoline N and –OH groups, running along the a-axis direction.[50] Aspirinate anions are also hydrogen bonded (with salt formation) to the most basic quinuclidine N atom of quininium cations. The overall shape of this packing motif could be compared to that of a rod. The intermolecular forces among adjacent chains, van der Waals and weak (non-classical) hydrogen bonds, are likely considerably weaker than the salt-forming hydrogen bonding interactions within the chains. This additionally suggests a possible chain rotational mobility (in the amorphous phase) approximately around the a-axis direction, without substantially disrupting the hydrogen bonding motif giving rise to the chains that also extend along that direction.

AFM studies have demonstrated that molecules in solids can be more mobile than traditionally expected.[73] Molecular mobility differences between the surfaces and the bulk of organic glasses have been also reported,[74] and the rates of amorphous recrystallization can be larger on particle surfaces.

Physicochemical properties such as polarity of the medium (dielectric constant), affect the strengths of electrostatic interactions, and together with molecular mobility, the ability of molecular ions to reorient themselves. Other molecular and solvent/vapour properties, such as protic donor or acceptor character, shape, size, *etc.* also play roles in determining energetically favourable intermolecular interactions, diffusion, and crystallization processes. DMF is a hydrogen bond acceptor and a polar compound, thus its intermolecular interactions with QA will be stronger than those of hexane. This is due to the dipole–ion and classical hydrogen bonds that would be enabled, in comparison with van der Waals and London dispersion forces mostly expected from hexane, a non-polar compound not forming classical hydrogen bonds. However, non-classical (weak) hydrogen bonds (from C–H bonds in hexane with electronegative atoms of QA) are still possible. The diffusional properties of hexane and DMF in QA particle surfaces and their bulk likely will differ as well, especially considering that DMF will dissolve QA (a salt) at least to some extent, while hexane is not expected to do so.

Conclusions

This work reports pioneering microED data and structural results (unit-cell parameters), demonstrating the presence of weakly diffracting nanocrystalline domains in quininium aspirinate prepared as an amorphous phase by neat manual grinding. The diffracting domains are estimated to exist at the nano-size scale, in otherwise amorphous bulk phases by XRPD. This result is significant to understand, at the single-particle level, the short- and long-range order features that can co-exist in organic amorphous phases. This work also illustrates microED's applicability toward the structural characterization of mechanochemically synthesized materials, typically as powders. The combined STEM and microED experiments are also fast; however, the powders must not decompose due to exposure to the electron beam, or under high vacuum.

For polymorphic organic systems, including economically significant small-molecule pharmaceuticals, the determination of the unit cell parameters of crystalline QA by microED studies of the amorphous solid is a very valuable result, suggesting an experimental methodology to anticipate the polymorphs that could recrystallize from so-called 'X-ray amorphous' phases, especially when these have been differently prepared.

This study also reports the recrystallization of amorphous QA upon exposure to vapours of DMF and hexane. DMF leads to an overall faster recrystallization process. The XRPD data of this product, once recrystallization is deemed complete, indicates a larger average crystalline domain size than for QA recrystallized from hexane vapours. On the contrary, amorphous QA recrystallization can be avoided by its storage in a closed container at ambient conditions, at around 75 K below its glass transition temperature. A brief discussion of these observations in terms of solubility differences and molecular mobility, phase transition energetics, crystal structure, and intermolecular interactions is provided.

Data availability

All experimental and characterization data and detailed experimental procedures are available in the published article and the ESI.‡ Experimental raw data is available at **https://data.mendeley.com/** under the title "MicroED, X-ray powder diffraction and optical microscopy raw data", DOI: **https://www.doi.org/10.17632/pc534rgswf.1**.

Conflicts of interest

There are no conflicts of interest to declare.

Acknowledgements

Notes and references

1 H. J. R. Lemmer, and W. Liebenberg, in *Crystal Growth and Chirality – Technologies and Applications*, ed. R. Marzouki and T. Akitsu, IntechOpen, 2022, pp. 1–13.

2 S. R. Byrn, R. R. Pfeiffer and J. G. Stowell, *Solid-State Chemistry of Drugs*, SSCI Inc, West Lafayette, Indiana, USA, 2nd edn, 1999.

3 R. J. Davey, S. L. M. Schroeder and J. H. Ter Horst, *Angew. Chem., Int. Ed.*, 2013, **52**, 2166–2179.

4 J. Zhou, Y. Zhou and W. Tang, *Crystals*, 2022, **12**(7), 980.

5 S. Karthika, T. K. Radhakrishnan and P. Kalaichelvi, *Cryst. Growth Des.*, 2016, **16**, 6663–6681.

6 R. Zallen, *The Physics of Amorphous Solids*, Wiley-VCH Verlag GmbH & Co., Weinheim, Germany, 2004.

7 J. G. Hernández and C. Bolm, *J. Org. Chem.*, 2017, **82**, 4007–4019.

8 J. Alić, M. C. Schlegel, F. Emmerling and T. Stolar, *Angew. Chem., Int. Ed.*, 2024, **63**, e202414745.

9 K. J. Ardila-Fierro and J. G. Hernández, *ChemSusChem*, 2021, **14**, 2145–2162.

10 S. Pagola, *Crystals*, 2023, **13**, 124.

11 P. A. Julien and T. Friščić, *Cryst. Growth Des.*, 2022, **22**, 5726–5754.

12 J. Alić, I. Lončarić, M. Etter, M. Rubčić, Z. Štefanić, M. Šekutor, K. Užarević and T. Stolar, *Phys. Chem. Chem. Phys.*, 2024, **26**, 4840–4844.

13 K. Linberg, B. Röder, D. Al-Sabbagh, F. Emmerling and A. A. L. Michalchuk, *Faraday Discuss.*, 2023, **241**, 178–193.

14 H. Spikes, *Friction*, 2018, **6**, 1–31.

15 J. Ribas-Ariño and D. Marx, *Chem. Rev.*, 2012, **112**, 5412–5487.

16 Y. S. Zholdassov, L. Yuan, S. R. Garcia, R. W. Kwok, A. Boscoboinik, D. J. Valles, M. Marianski, A. Martini, R. W. Carpick and A. B. Braunschweig, *Science*, 2023, **380**, 1053–1058.

17 A. Khawam and D. R. Flanagan, *J. Phys. Chem. B*, 2006, **110**, 17315–17328.

18 T. Friščić, I. Halasz, P. J. Beldon, A. M. Belenguer, F. Adams, S. A. Kimber, V. Honkimaki and R. E. Dinnebier, *Nat. Chem.*, 2013, **5**, 66–73.

19 K. Užarević, I. Halasz and T. Friščić, *J. Phys. Chem. Lett.*, 2015, **6**, 4129–4140.

20 S. Lukin, K. Užarević and I. Halasz, *Nat. Protoc.*, 2021, **16**, 3492–3521.

21 D. Gracin, V. Štrukil, T. Friščić, I. Halasz and K. Užarević, *Angew. Chem., Int. Ed.*, 2014, **53**, 6193–6197.

22 H. Kulla, S. Haferkamp, I. Akhmetova, M. Röllig, C. Maierhofer, K. Rademann and F. Emmerling, *Angew. Chem., Int. Ed.*, 2018, **57**, 5930–5933.

23 T. Friščić and W. Jones, *Cryst. Growth Des.*, 2009, **9**, 1621–1637.

24 S. L. James, C. J. Adams, C. Bolm, D. Braga, P. Collier, T. Friščić, F. Grepioni, K. D. M. Harris, G. Hyett, W. Jones, A. Krebs, J. Mack, L. Maini, A. G. Orpen, I. P. Parkin, W. C. Shearouse, J. W. Steed and D. C. Waddell, *Chem. Soc. Rev.*, 2012, **41**, 413–447.

25 S. Mohamud, V. Ta Phuoc, N. E. Massa and S. Pagola, *Synth. Met.*, 2016, **214**, 71–75.

26 J. Jones, V. Ta Phuoc, L. Del Campo, N. E. Massa, C. M. Brown and S. Pagola, *Cryst. Growth Des.*, 2019, **19**, 4970–4980.

27 S. H. Lapidus, A. Naik, A. Wixtrom, N. E. Massa, V. Ta Phuoc, L. Del Campo, S. Lebègue, J. G. Ángyán, T. Abdel-Fattah and S. Pagola, *Cryst. Growth Des.*, 2014, **14**, 91–100.

28 A. Doerr, *Nat. Methods*, 2014, **11**, 6–7.

29 K. D. Corbett and M. A. Herzik, *Nat. Methods*, 2022, **19**, 652–653.

30 B. L. Nannenga, D. Shi, A. G. W. Leslie and T. Gonen, *Nat. Methods*, 2014, **11**, 927–930.

31 E. Danelius, K. Patel, B. Gonzalez and T. Gonen, *Curr. Opin. Struct. Biol.*, 2023, **79**, 102549.

32 I. Nederlof, E. Van Genderen, Y. W. Li and J. P. Abrahams, *Acta Crystallogr., Sect. D:Biol. Crystallogr.*, 2013, **69**, 1223–1230.

33 P. Simoncic, E. Romeijn, E. Hovestreydt, G. Steinfeld, G. Santiso-Quiñones and J. Merkelbach, *Acta Crystallogr., Sect. E:Struct. Rep. Online*, 2023, **79**, 410–422.

34 C. G. Jones, M. W. Martynowycz, J. Hattne, T. J. Fulton, B. M. Stoltz, J. A. Rodriguez, H. M. Nelson and T. Gonen, *ACS Cent. Sci.*, 2018, **4**, 1587–1592.

35 C. G. Jones, M. Asay, L. J. Kim, J. F. Kleinsasser, A. Saha, T. J. Fulton, K. R. Berkley, D. Cascio, A. G. Malyutin, M. P. Conley, B. M. Stoltz, V. Lavallo, J. A. Rodríguez and H. M. Nelson, *ACS Cent. Sci.*, 2019, **5**, 1507–1513.

36 T. Sasaki, T. Nakane, A. Kawamoto, T. Nishizawa and G. Kurisu, *CrystEngComm*, 2022, **25**, 352–356.

37 L. R. Doyle, E. A. Thompson, A. L. Burnage, A. C. Whitwood, H. T. Jenkins, S. A. Macgregor and A. S. Weller, *Dalton Trans.*, 2022, **51**, 3661–3665.

38 D. Gogoi, T. Sasaki, T. Nakane, A. Kawamoto, H. Hojo, G. Kurisu and R. Thakuria, *Cryst. Growth Des.*, 2023, **23**, 5821–5826.

39 J. Lin, J. Unge and T. Gonen, *Adv. Sci.*, 2023, **10**, 1–5.

40 G. Bu, E. Danelius, L. H. E. Wieske and T. Gonen, *Adv. Biol.*, 2024, **8**, 6–11.

41 T. Yang, S. Waitschat, A. K. Inge, N. Stock, X. Zou and H. Xu, *Symmetry*, 2021, **13**, 2131.

42 P. B. Klar, Y. Krysiak, H. Xu, G. Steciuk, J. Cho, X. Zou and L. Palatinus, *Nat. Chem.*, 2023, **15**, 848–855.

43 I. B. Rietveld, F. Painsecq, C. Jandl, D. Stam and G. Coquerel, *Cryst. Growth Des.*, 2024, **24**, 5893–5897.

44 M. Descamps and J. F. Willart, *Adv. Drug Delivery Rev.*, 2016, **100**, 51–66.

45 J. F. Willart and M. Descamps, *Mol. Pharm.*, 2008, **5**, 905–920.

46 N. S. Trasi and S. R. Byrn, *AAPS PharmSciTech*, 2012, **13**, 772–784.

47 S. Bates, G. Zografi, D. Engers, K. Morris, K. Crowley and A. Newman, *Pharm. Res.*, 2006, **23**, 2333–2349.

48 L. Yu, *Adv. Drug Delivery Rev.*, 2001, **48**, 27–42.

49 Z. Chen, K. Higashi, K. Ueda and K. Moribe, *Nano Lett.*, 2022, **22**, 6841–6846.

50 N. Harris, J. Benedict, D. A. Dickie and S. Pagola, *Acta Crystallogr., Sect. C:Struct. Chem.*, 2021, **77**, 566–576.

51 Bruker AXS GmbH:7.0.

52 A. Bhakar, M. Taxak and S. Kumar Rai, *J. Appl. Crystallogr.*, 2023, **56**, 1466–1479.

53 A. C. Larson and R. B. vonDreele, *Los Alamos National Laboratory Report*, 2004, pp. 86–748.

54 *Golden Software*, LLC:12.7.855 (64-bit).

55 *ELDICO Scientific*, AG:1.4.2.

56 *Bruker AXS GmbH*, 2012.

57 T. Ungár and J. Gubicza, *Z. Kristallogr.*, 2007, **222**, 114–128.

58 J. Zhao, H. Xu, H. Lebrette, M. Carroni, H. Taberman, M. Högbom and X. Zou, *Nat. Commun.*, 2021, **12**, 5036.

59 N. Vlahakis, J. Holton, N. K. Sauter, P. Ercius, A. S. Brewster and J. A. Rodriguez, *Annu. Rev. Phys. Chem.*, 2024, **116**, 483–508.

60 T. G. Fawcett, S. Gates-Rector, A. M. Gindhart, M. Rost, S. N. Kabekkodu, J. R. Blanton and T. N. Blanton, *Powder Diffr.*, 2019, **34**, 164–183.

61 C. F. Holder and R. E. Schaak, *ACS Nano*, 2019, **13**, 7359–7365.

62 A. Le Bail, *Powder Diffr.*, 2005, **20**, 316–326.

63 S. Nakamatsu, S. Toyota, W. Jones and F. Toda, *Chem. Commun.*, 2005, 3808–3810.

64 A. Jayasankar, D. J. Good and N. Rodríguez-Hornedo, *Mol. Pharm.*, 2007, **4**, 360–372.

65 D. Braga, G. S. Luca, F. Grepioni, M. R. Chierotti, R. Gobetto, G. Palladino and M. Polito, *CrystEngComm*, 2007, **9**, 879–881.

66 I. Huskić, C. B. Lennox and T. Friščić, *Green Chem.*, 2020, **22**, 5881–5901.

67 A. Newman and G. Zografi, *J. Pharm. Sci.*, 2019, **108**, 1061–1080.

68 G. A. Bowmaker, *Chem. Commun.*, 2013, **49**, 334–348.

69 A. V. Raut, S. A. Jadhav, D. R. Shengule and K. M. Jadhav, *J. Sol-Gel Sci. Technol.*, 2016, **79**, 1–11.

70 G. K. Williamson and W. H. Hall, *Acta Metall.*, 1953, **1**, 22–31.

71 B. Himabindu, N. S. M. P. Latha Devi and B. Rajini Kanth, *Mater. Today: Proc.*, 2021, **47**, 4891–4896.

72 N. Hirota, Y. Hattori and M. Otsuka, *Adv. Powder Technol.*, 2016, **27**, 808–811.

73 G. Kaupp, *CrystEngComm*, 2003, **5**, 117–133.

74 L. Zhu, C. W. Brian, S. F. Swallen, P. T. Straus, M. D. Ediger and L. Yu, *Phys. Rev. Lett.*, 2011, **106**, 1–4.